Supplementary Information for

Eco-sustainable biosynthesis of $CoFe_2O_4$ nanoparticles using apple extract for multifunctional applications

Heba Hussein*[a], S. S. Ibrahim[a], Sherif A. Khairy[a]

[a] Physics Department, Faculty of Science, Cairo University, Cairo-11566, Egypt

*Corresponding author, Email: Heba@sci.cu.edu.eg

Experimental work

Materials and Chemicals

Table S1: Materials and chemicals used in this study.

Chemical/Reagent	Molecular Weight (g/mol)	Purity (%)	Source
Iron (III) nitrate nonahydrate	404.00	> 98	Chem Lab NV, Belgium
Cobalt (II) nitrate hexahydrate	291.03	> 98	Loba, India
Oxalic acid anhydrous	90.03	98	Loba, India
Lead (II) nitrate	331.21	> 99	Loba, India
Chromium (III) nitrate nonahydrate	400.15	> 99	Loba, India
Egyptian Apple	-	-	Egyptian markets

Preparation Steps for Apple Extract

1. Thoroughly wash apples with distilled water to ensure cleanliness.
2. Peel the apples and cut them into small cubes.
3. Weigh 50 g of apple cubes and place them in 100 ml of distilled water.
4. Stir the mixture using a magnetic stirrer at 650 rpm for 1 hour at room temperature (T_r).
5. Heat the mixture to a boiling temperature of 100 °C while continuously stirring at the same speed for an additional hour.
6. Allow the mixture to cool naturally to room temperature after boiling.
7. Filter the cooled solution three times using Whatman No. 1 filter paper to obtain a pure extract.
8. A schematic representation of these preparation steps is provided in **Fig. S1**.

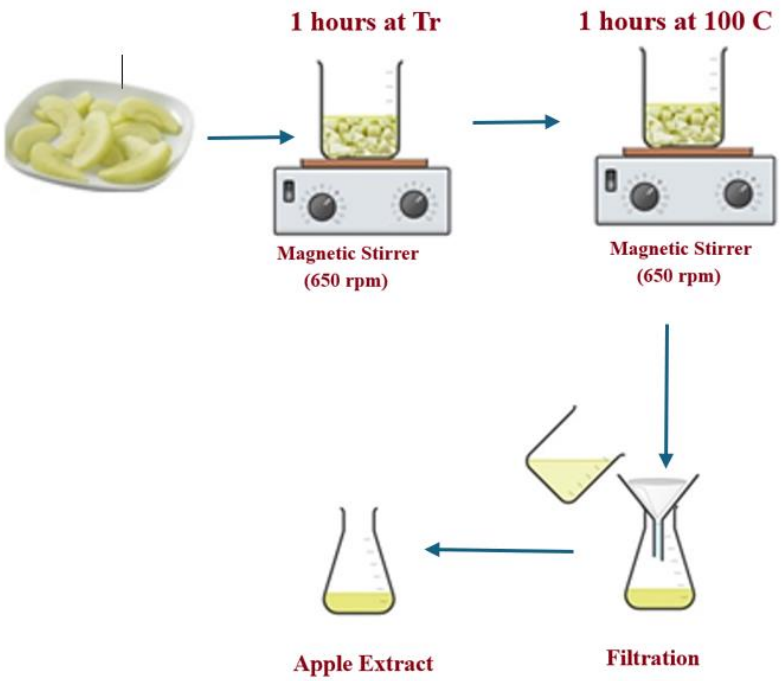

Fig. S1 Schematic representation of the preparation for apple extract.

Synthesis of $CoFe_2O_4$ Nanoparticles

$CoFe_2O_4$ nanoparticles were synthesized via a self-combustion (self-ignition) process using a prepared extract rich in carboxylic acids (phenolic acids) and flavonoids (phenolic compounds). In this process, specific concentrations of metal nitrates were carefully and slowly added in powder form to a predetermined volume of the extract under magnetic stirring. The resulting solution was then heated at 100 °C to evaporate water, concentrating it into a brown viscous gel. This gel was subsequently heated to 350 °C, during which it first melted and then spontaneously decomposed through auto-combustion; as the phenolic acids and flavonoids decomposed, gases such as carbon (or carbon dioxide) and nitrogen dioxide were released, leaving behind burnt magnetic foams (**Fig. S2**). These as-burned foams were ground into a fine powder using an agate mortar, and to enhance crystallinity, the powder was sintered in the air using a Nabertherm furnace (LH 60/12).

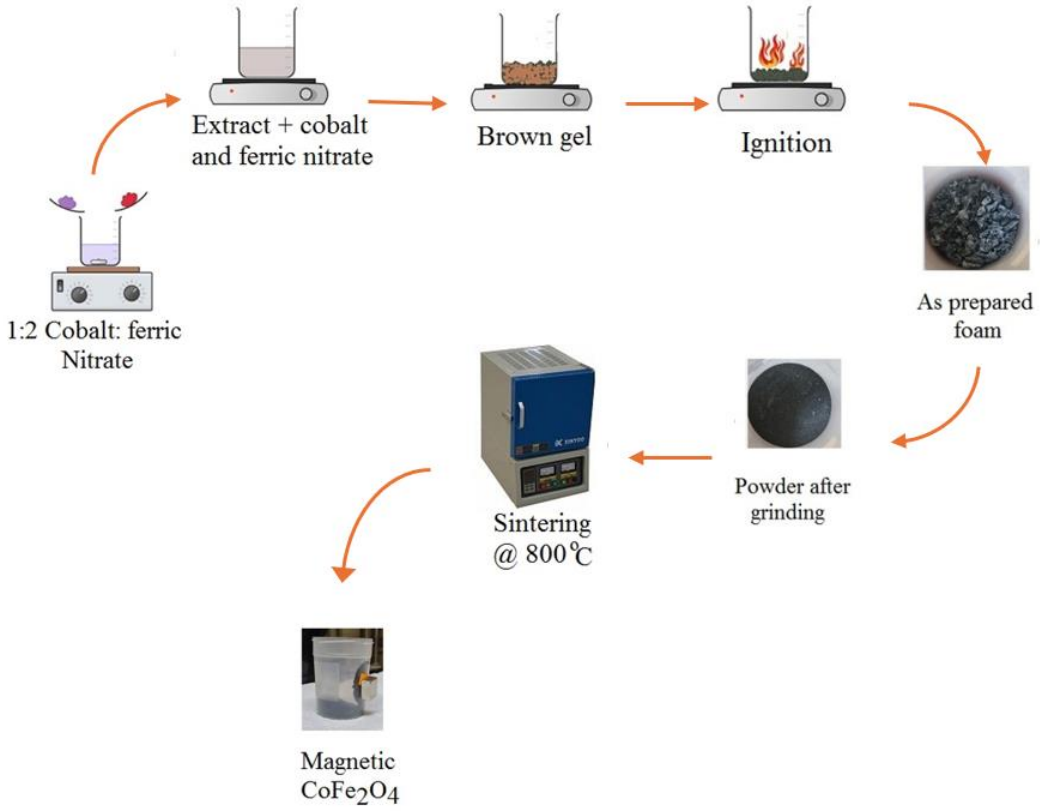

Fig. S2 Schematic representation of the preparation of $CoFe_2O_4$ nanoparticles using apple extract.

The $CoFe_2O_4$ ferrite sample prepared using apple extract (Co-A) was synthesized according to the preparation conditions provided in **Table S2.** The conditions for the preparation of the sample were selected (optimized) via several trials to obtain a single and pure phase of $CoFe_2O_4$ ferrite nanoparticles.

Table S2: Details of the sample preparation conditions.

Condition parameter	Information
Concentration of extract	50%
Volume of extract	25 ml
Concentration of metals (Fe^{3+}: Co^{2+})	2:1
Stirring time	15 min
Stirring rate	650 rpm
Grinding time	5 min
Sintering temperature	800 °C
Sintering time	1 h
Heating/Cooling rate	4 °C/min

Analysis and Characterization

a) High-performance liquid chromatography (HPLC)

A qualitative analysis of the apple extract utilized in the synthesis was performed using a Waters 2690 Alliance HPLC system equipped with a photodiode array detector (Waters 996 PDA) set to 280 nm. The system operated with an injection volume of 10 µL, a flow rate of 1 µL/min, and a column oven temperature maintained at 25 °C. Methanol was employed to prepare stock standards, which were filtered using 0.22 µm syringe filters. The solvents of the mobile phases consisted of acetonitrile and 0.1% phosphoric acid in water.

b) X-ray diffraction (XRD) analysis

The crystal structure of $CoFe_2O_4$ nanoparticles was analyzed using an X'Pert PRO-PANalytical X-ray diffractometer with Cu-Kα radiation (λ = 1.5406 Å) channel control (with secondary monochromator Holland radiation and a 45 kV tube). Data were collected over a 2θ range of 16°–80° at room temperature. Rietveld profile analysis, performed using FullProf.2k software (version 7.95 - Jan 2023 - ILL-JRC), provided detailed insights into the crystal structure and microstructure

c) Fourier transform infrared measurements (FTIR) spectroscopy

FTIR analysis was conducted with a SHIMADZU model IRAffinity-1 instrument spectrophotometer equipped with an attenuated total reflection unit (ART), covering the range of 900–300 cm^{-1}.

d) Raman spectroscopy

The Raman spectrum of the nanoparticles was recorded using a Horiba LabRam HR Evolution spectrometer (Horiba, Ltd., UK) within the 170–720 cm^{-1} range at room temperature.

e) Field emission scanning electron microscope (FESEM)

The morphology of the nanoparticles was examined using a Quanta 250 FESEM with FEG FEI, USA, operated at 20–30 kV.

f) High-resolution transmission electron microscope (HRTEM)

HRTEM analysis, using a microscope (JEOL JEM2100 series, Tokyo, Japan), determined particle size and shape. The rings of the SAED pattern were indexed with the C Spot program (Trial version 2.0). This program also calculates the interplanar spacings (distances). The particle size distribution was assessed with ImageJ (fifty particles were counted from the TEM images) and OriginLab software. The sample's crystal structure and associated particles were identified using the Smorf crystal model program.

g) X-ray photoelectron spectroscopy (XPS)

XPS was performed to identify the oxidation states of elements using a surface science instrument (Thermo Fisher Scientific instrument, USA), with Al Kα monochromatic radiation (10 to 1350 eV) spot size of 400 mm at a pressure of 10^{-9} m bar with a full spectrum pass energy of 200 eV and a narrow spectrum of 50 eV. Gaussian-Lorentzian (GL) peak fitting was conducted using Avantage Data Spectrum Processing™. A smart background approach is used to correct the baselines. The C (1S) peak, fixed at 284.8 eV, served as the reference point for the binding energies..

h) Magnetic measurements

The magnetic hysteresis loop of the nanoparticles was obtained at room temperature using a vibrating sample magnetometer (VSM, Lake Shore model 7410) under a 20 kOe field.

i) Mössbauer spectroscopy

^{57}Fe Mössbauer spectra were acquired at room temperature using a standard constant acceleration transmission spectrometer with a ^{57}Co in the α Rh matrix γ-source as the Mössbauer source. The recorded spectra were analyzed using a nonlinear least-squares fitting approach, assuming a Gaussian profile. The Mössbauer parameters were then extracted relative to a calibrated reference spectrum of metallic α-iron. The maximum Doppler velocity for the measurements was set at 10 mm/s.

j) UV–VIS-NIR spectroscopy measurement

The optical properties of the nanoparticles were analyzed using a Jasco-V-770, Japan spectrophotometer with an integrating sphere reflectance unit (ISN) in the 190–2400 nm wavelength range.

k) Brunauer–Emmett–Teller (BET) analysis

The specific surface area and pore size distribution were measured using nitrogen adsorption-desorption isotherms at 77 K on a Nova 2000 series Quantachrome instrument (USA), using the BET Multipoint method.

l) Water treatment (heavy metal removal)

To evaluate the effectiveness of cobalt ferrite in removing heavy metals (Cr^{3+} and Pb^{2+}) from water and to identify the optimal pH for adsorption, 0.02 g of cobalt ferrite was introduced into a 50 ppm heavy metal standard solution. The mixture was agitated using a custom orbital shaker, and its pH was adjusted between 2 and 8 using NaOH and HCl. After 30 minutes, the clarified solutions were filtered through a 0.22 µm syringe filter and analyzed via inductively coupled plasma mass spectrometry (ICP-MS) using an iCAP-Qc instrument (Thermo Fisher Scientific, USA).

To determine the optimal adsorbent dosage, the experiment was repeated at the previously identified ideal pH while varying the amount of cobalt ferrite from 0.02 to 0.12 g.

Finally, to establish the most effective contact time, the experiment was conducted again using the optimized pH and adsorbent dosage. The contact time was systematically varied between 10 and 60 minutes, and the resulting solutions were analyzed using ICP-MS.

The removal efficiency of cobalt ferrite was calculated using the following equation [1]:

$$Removal\ efficiency\ \% = \frac{c_0 - c_f}{c_0} \times 100 \quad \text{S1}$$

where c_0 is the initial concentration of the heavy metal solution (ppm), and c_f denotes the final concentration after adsorption (ppm).

Following the adsorption process, $CoFe_2O_4$ nanoparticles were separated from the heavy metal-containing solution using a magnet. To prepare them for reuse, the nanoparticles were thoroughly washed multiple times with acetone, 0.01 M HCl, and distilled water. This regeneration process allowed the cobalt ferrite to be reused in subsequent adsorption experiments for up to four cycles. The objective was to assess the reusability of the green-synthesized cobalt ferrite in removing Pb^{2+} and Cr^{3+} from aqueous solutions.

m) Statistical analysis

To evaluate the impact of pH, contact time, and adsorbent dosage on heavy metal removal, an analysis of variance (ANOVA) was performed using Minitab 17 in triplicate at a 95% confidence level. Tukey's Honestly Significant Difference (HSD) test was applied to determine statistically significant differences between group means.

n) Photo-Fenton Catalytic Degradation

To initiate the photo-Fenton catalytic process, a 9W Phillips visible light (VIS) lamp was used to illuminate a solution containing 0.15 g/L of catalyst, 250 mL of 9.37×10^{-5} M L^{-1} methylene blue (MB), and 1.5×10^{-3} M L^{-1} oxalic acid. The mixture was continuously stirred using a homemade mechanical stirrer for 30 min in the dark for adsorption-desorption equilibrium. After that, the incident visible light was directed vertically onto the solution surface from a distance of 12 cm under continuous stirring for 2 hours for the photo-Fenton catalytic degradation process. At regular intervals (10 min), 5 mL aliquots of the MB dye solution were withdrawn, and the catalyst was extracted from the mixture using a permanent magnet. The variation in MB concentration throughout the reaction was analyzed using a Shimadzu 2401 UV-Vis spectrometer set to a wavelength of 665 nm. The following equation [2] was used to estimate the percentage of dye removal or dye degradation efficiency after the retention period:

$$\%Degradation = \left(1 - \frac{C_t}{C_o}\right) \times 100 \quad \text{S2}$$

where C_0 represents the initial concentration of MB dye before irradiation, and C_t is the final concentration of MB dye after the irradiation time, t.

After a photo-Fenton catalytic degradation experiment, the $CoFe_2O_4$ nanoparticles were recovered from the solution containing MB dye and oxalic acid using a permanent magnet. The nanoparticles were then thoroughly washed with acetone, 0.01 M HCl, and distilled water multiple times. This process was repeated before reusing the nanoparticles in subsequent experiments, up to five cycles, to test the reusability of cobalt ferrite for photo-Fenton catalytic degradation activity.

X-ray diffraction (XRD)

Rietveld refinement

Table S3: Positions, atomic coordinates, isotropic coefficients, and site occupancy factors (SOFs) for each cation and anion for the Co-A nanoparticles.

Parameters	Atoms	Wyckoff positions	Atomic coordinates			B(ISO)	SOF
			x/a	y/b	z/c		
Values	O1	32e	0.25597	0.25597	0.25597	0.00000	0.17436
	FeO[b]	16d	0.50000	0.50000	0.50000	0.00000	0.05123
	CoO[b]	16d	0.50000	0.50000	0.50000	0.00000	0.03107
	FeT[a]	8a	0.12500	0.12500	0.12500	0.00000	0.03107
	CoT[a]	8a	0.12500	0.12500	0.12500	0.00000	0.00958

T[a] stands to tetrahedral site
O[b] stands to octahedral site

R-factors such as the Bragg factor (R_B), crystallographic factor (R_F), expected profile factor (R_{exp}), weighted profile factor (R_w), and goodness of fit (GOF) are calculated using the following equations [3-5] and are listed in **Table S4**.

$$R_B = \frac{\sum(I_{Obs} - I_{Cal})}{\sum I_{Obs}} \quad \text{S3}$$

$$R_w = \frac{\sum w_i \sqrt{(I_{Obs} - I_{Cal})^2}}{\sum w_i I_{Obs}^2} \quad \text{S4}$$

$$R_{exP} = \left[\frac{N-P}{\sum w_i I_{Obs}^2}\right]^2 \quad \text{S5}$$

$$GOF = \frac{R_w}{R_{exp}} \quad \text{S6}$$

where I_{Obs} and I_{Cal} are the corresponding experimental and calculated intensities. In addition, N is the number of experimental observations, w_i ($1/I_{Obs}$) is the weight, and P is the total number of fitting parameters.

The Debye-Scherrer equation is used for estimating the average crystallite size and is given by:

$$D = \frac{K\lambda}{\beta cos\theta} \quad \text{S7}$$

where K is the shape factor (~0.9), λ is the X-ray wavelength, β is the peak's FWHM, and θ is the Bragg angle.

The equation that defines the dislocation [6] in terms of the length of the dislocation lines per unit volume of the crystal lattice is given by:

$$\delta_d = {}^{1}/_{D^2} \quad \text{S8}$$

where D is the crystallite size of the sample.

Additionally, the microstrain is calculated using the formula [7]:

$$\varepsilon = \frac{\beta}{4tan\theta} \quad \text{S9}$$

where θ is the FWHM and β is the diffraction angle.

The volume of the prepared sample (**Table S4**) can be expressed as:

$$V = a^3 \quad \text{S10}$$

The distortion of the crystalline structure was indicated by the tolerance factor (T). Oxygen ionic radius (R_o=1.38Å)[8], octahedral site radius (r_B), and tetrahedral site radius (r_A) values were used to calculate the tolerance factor (T) of the synthesized cobalt ferrite nanoparticles according to the following equation [9]:

$$T = \frac{1}{\sqrt{3}}\left(\frac{r_A + R_o}{r_B + R_o}\right) + \frac{1}{\sqrt{2}}\left(\frac{R_o}{r_A + R_o}\right) \quad \text{S11}$$

The tolerance factor is unity for an ideal spinel structure [10].

Furthermore, the bulk density (ρ_B) was calculated using the following equation [11]:

$$\rho_B = \frac{m}{\pi r^2 h} \quad \text{S12}$$

where m (g), r (cm), and h (cm) are the mass, radius, and thickness of the pellet, respectively.

The X-ray density (ρ_x), was used to investigate the changes in the crystal structure of crystalline materials. The equation used to compute the theoretical or X-ray density from the diffractograms is as follows [11]:

$$\rho_x = \frac{ZM_w}{N_A a^3} \quad \text{S13}$$

where N_A is Avogadro's number, Z is the number of atoms per unit cell (Z=8) [12], M_w is the molecular weight (M_w = 234.625g/mole), and a is the lattice constant.

The porosity (P_o%) of eco-friendly Co-A nanoparticles can be expressed as [11]:

$$P_o\% = \left(1 - \frac{\rho_B}{\rho_x}\right) \times 100 \quad \text{S14}$$

Table S4: Crystal structure, space group, lattice constant (a), angle (α, β, and γ), unit cell volume (V), tolerance factor (T), X-ray density (ρ_X), bulk density (ρ_B), porosity% (P_o%), average crystallite size (D) according to the Scherrer method, dislocation density (δ_d), internal microstrain, (ε), agreement factor (R_B%), (R_F%), (R_w), (R_{exp}), (GOF), (χ^2), and the cation distribution from the Rietveld structure refinement of the eco-friendly Co-A nanoparticles.

Parameters	Values
Crystal structure	Cubic
Space group	Fd3̄m
a (Å)/ b (Å)/ c (Å)	8.372
V(Å)^3	586.730
α °/ β °/ γ °	90
Tolerance factor, (T)	0.998
X-Ray density, ρ_X (g/cm^3)	5.312
Bulk density, ρ_B (g/cm^3)	4.020
Porosity%, (P_o%)	23.96%
D (nm)	27.820
Dislocation density, (δ_d) (Lines.nm^{-2})	0.001
Internal microstrain, (ε)	3.450×10^{-4}
R_B (%)	5.530
R_F (%)	4.620
R_{exp}	12.800
R_w	14.300
GOF	1.120
χ^2	1.090
Cation Distribution	$(Co_{0.23}Fe_{0.77})_A(Co_{0.77}Fe_{1.23})_B$

The mean ionic radius per molecule at the tetrahedral and octahedral sites is determined by the cation distributions using the following equations [13]:

$$r_A = x r_{M(A)} + (1-x) r_{Fe(A)} \quad \text{S15}$$

$$r_B = {}^1/_2 \left[(1-x) r_{M(B)} + (1+x) r_{Fe(B)}\right] \quad \text{S16}$$

where $r_{M(A)}$, $r_{M(B)}$, $r_{Fe(A)}$, and $r_{Fe(B)}$ are the radii of the metal cations (Co^{2+}) and (Fe^{3+}) ions at the A and B sites, respectively, and x denotes the fractional content of metal ions at both tetrahedral and octahedral sites.

The mean interionic distances (bond lengths) at the tetrahedral (r_t) and octahedral (r_o) sites are estimated using the following relationships [14]:

$$r_t = a\sqrt{3}\left(u^{43m} - \frac{1}{4}\right) - R_o \quad \text{S17}$$

$$r_o = a\left(\frac{5}{8} - u^{43m}\right) - R_o \quad \text{S18}$$

where a, u^{43m}, and R_o are the experimental lattice constant, the oxygen position parameter, and the oxygen ionic radius, respectively.

Additionally, the shared tetrahedral edge length (d_{AE}), shared octahedral edge length (d_{BE}), unshared octahedral edge length (d_{BEu}), bond length at tetrahedral sites (d_{AL}), and bond length at octahedral sites (d_{BL}) for the cobalt ferrite sample are determined using the following relationships [15, 16]:

$$d_{AE} = a\sqrt{2}\,(2u^{43m} - 0.5) \quad \text{S19}$$

$$d_{BE} = a\sqrt{2}\,(1 - 2u^{43m}) \quad \text{S20}$$

$$d_{BEU} = a\sqrt{\left(4(u^{43m})^2 - 3(u^{43m}) + \frac{11}{16}\right)} \quad \text{S21}$$

$$d_{AL} = a\sqrt{3}\,\left(\delta + \frac{1}{8}\right) \quad \text{S22}$$

$$d_{BL} = a\sqrt{\left(3\delta^2 - \left(\frac{\delta}{2}\right) + \left(\frac{1}{16}\right)\right)} \quad \text{S23}$$

where δ is the deviation of the oxygen position parameter from its ideal value, which can be given as [17]:

$$\delta = u - u_{ideal} \quad \text{S24}$$

Table S5: The values of the mean ionic radius per molecule at tetrahedral and octahedral sites (r_A), (r_B), oxygen position parameters (u^{3m}), ($u4^{3m}$), (δ), mean interionic distance at tetrahedral and octahedral sites (r_t), (r_o), shared tetrahedral edge length (d_{AE}), shared octahedral edge length (d_{BE}), unshared octahedral edge length (d_{BEU}), tetrahedral bond length (d_{AL}), octahedral bond length (d_{BL}), experimental lattice constant (a_{exp}), and theoretical lattice constant (a_{th}) for the Co-A sample.

Parameters	Values (Å)
r_A	0.511
r_B	0.684
Oxygen Position Parameter (U)	
u^{3m}	0.256
u^{3m} ideal	0.250
u^{43m}	0.381
u^{43m} ideal	0.375
δ	0.006
Bond Lengths	
r_t	0.519
r_o	0.663
d_{AE}	3.101
d_{BE}	2.819
d_{BEu}	2.962
d_{AL}	1.899
d_{BL}	2.044
Lattice Constants	
a_{exp}	8.372
a_{th}	8.414

The relationship between ionic radius and lattice constant is well-established. The formula proposed by Mazen et al. [18] allows for the calculation of the theoretical lattice constant:

$$a_{th} = \frac{8}{3\sqrt{3}}\left[(r_A + R_o) + \sqrt{3}(r_B + R_o)\right] \quad \text{S25}$$

where r_A, r_B, and R_o represent the mean ionic radii per molecule at the tetrahedral and octahedral sites and the radius of the oxygen ions, respectively.

Table S6: Used equation of the bond angles, cation–cation (Me–Me) and cation-anion (Me–O) distances [19].

(Me-Me) bond distance	(Me-O) bond distance	Bond angle
$b = \sqrt{2}(a/4)$	$p = a\left(\frac{1}{2} - u^{3m}\right)$	$\theta_1 = \mathrm{Cos}^{-1}\left(\frac{p^2 + q^2 - c^2}{2pq}\right)$
$c = \sqrt{11}(a/8)$	$q = a\sqrt{3}\left(u^{3m} - \frac{1}{8}\right)$	$\theta_2 = \mathrm{Cos}^{-1}\left(\frac{p^2 + r^2 - e^2}{2pr}\right)$
$d = \sqrt{3}(a/4)$	$r = a\sqrt{11}\left(u^{3m} - \frac{1}{8}\right)$	$\theta_3 = \mathrm{Cos}^{-1}\left(\frac{2p^2 - b^2}{2p^2}\right)$
$e = 3\sqrt{3}(a/8)$	$s = a\frac{\sqrt{3}}{3}\left(u^{3m} + \frac{1}{2}\right)$	$\theta_4 = \mathrm{Cos}^{-1}\left(\frac{p^2 + s^2 - f^2}{2ps}\right)$
$f = \sqrt{6}(a/4)$		$\theta_5 = \mathrm{Cos}^{-1}\left(\frac{r^2 + q^2 - d^2}{2rq}\right)$

Table S7: Estimated interionic bond lengths and bond angles of the prepared cobalt ferrite nanoparticles.

Parameters	Values
Cation-anion distances (Me-O) (Å)	
P (B-O)	2.043
q (A-O)	1.899
r (A-O)	3.637
s (B-O)	3.654
Cation-cation distances (Me-Me) (Å)	
b (B-B)	2.959
c (A-B)	3.471
d (A-A)	3.625
e (A-B)	5.438
f (B-B)	5.127
Bond angles(degree)	
(A-B)	
θ_1	123.413
θ_2	145.067
(B-B)	
θ_3	92.887
θ_4	125.730
(A-A)	
θ_5	74.504

Texture coefficient

The Harris method was used to determine TCs from the XRD data [20-22]:

$$TC_{(hkl)}=\frac{I_{hkl}/I_{0_{hkl}}}{1/n\ \sum_{i=0}^{n}\left(I_{hkl}/I_{0_{hkl}}\right)} \quad \text{S26}$$

where $TC_{(hkl)}$ is the texture coefficient for the reflection (hkl), $I_{(hkl)}$ is the measured relative diffraction intensity of a given (hkl) plane, $I_{o(hkl)}$ is the standard peak intensity for the reflection of the same plane based on the Joint Committee for Powder Diffraction Standards (JCPDS) reference card (01-080-6487), and n is the number of reflections observed in the XRD pattern. When $0 < TC_{(hkl)} < 1$, there was a lack of grains aligned in that direction. If $TC_{(h\,k\,l)} \approx 1$ for all the considered (h k l) planes, then the particles are randomly oriented crystallites, which is comparable to JCPDS references. An abundance of grains was created in a specific [h k l] direction if the values of $TC_{(hkl)}$ were greater than 1. The preference for crystallite formation in the direction perpendicular to the (h k l) plane increases as $TC_{(hkl)}$ increases.

Table S8: Texture coefficients for significant (hkl) planes of the eco-friendly Co-Acobalt ferrite nanoparticles

Miller indices (hkl)	Texture coefficient (TC)
111	**1.653**
220	0.969
311	0.741
222	1.235
400	0.900
422	0.833
511	0.718
440	0.775
531	0.568
620	1.268
533	1.076
622	0.969
444	1.295

Electron density

By applying the Fourier transform to the geometrical structural factor across the entire unit cell, it generates the electron density distribution [9]. This is given by [23]:

$$\rho(xyz)\frac{1}{V}\sum_{hkl} hkl\,|F_{hkl}|exp\{-2\pi i(hx+ky+lz-\alpha_{hkl})\} \quad \text{S27}$$

The electron density ρ(xyz) represents the electron distribution at the x-, y-, and z-coordinates within the unit cell volume (V). It is calculated using the measured amplitude of the structure factor F_{hkl}, with α_{hkl} as the phase angle corresponding to each Bragg reflection plane (hkl).

Fourier Transform Infrared (FTIR) Spectroscopy

The formula used to calculate Θ_D is as follows [24]:

$$\Theta_D = \frac{hc\nu_{av}}{2\pi\kappa_B} = 1.438\nu_{av} \quad \text{S28}$$

where h is Planck's constant (6.626×10^{-34} J.s), ν_{av} is the average wavenumber, K_B is Boltzmann's constant (1.38×10^{-23} J/K), and c is the velocity of light (2.99×10^8 m s^{-1}). The value of ($hc/2\pi K_B$) for ferrite materials is 1.438.

Anderson's formula [25] can also be used to calculate the Debye temperature (θ_D):

$$\theta_D = \frac{h}{k_B}\left(\frac{3Z\rho_x N_{AV}}{4\pi M}\right)^{\frac{1}{3}} \times V_m \quad \text{S29}$$

where h is Planck's constant, V_m is the mean wave velocity, K_B is Boltzmann's constant, N_{AV} is Avogadro's number (6.022×10^{23} mol^{-1}), M_w is the molecular weight of cobalt ferrite (234.62 g/mole), Z is the number of atoms in the unit formula, and ρ_x is the X-ray density.

The threshold energy (E_{th}) is determined from the FTIR spectra, as demonstrated by Waldron:

$$E_{th} = hc\nu_{th} \quad \text{S30}$$

where c is the speed of light and h is the Planck constant.

The simplified version of the force constants (K_O for B-site and K_T for A-site) in terms of the molecular weight of the cations on the A- and B-sites and the position of the absorption band is given by:

$$K_T = 7.62 \times M_A \times \nu_A^2 \times 10^{-7} \quad \text{S31}$$

$$K_O = 5.31 \times M_B \times \nu_{AB}^2 \times 10^{-7} \quad \text{S32}$$

where M_A and M_B are the molecular weights of the cations at the A- and B-sites, respectively.

The stiffness constants (according to Waldron [26] for cubic symmetry systems with an isotropic nature, $C_{11} = C_{12}$), bulk modulus (B), Young's modulus (E), rigidity modulus (G), Poisson's ratio (σ), longitudinal wave velocity (V_l), transverse wave velocity (V_t), and mean velocity (V_m) are calculated for the green-synthesized $CoFe_2O_4$ ferrite sample using the following equations [26-32]:

Stiffness constant $C_{11} = \frac{K_{av}}{a}$ S33

Bulk modulus $B = \frac{1}{3}(C_{11} + 2C_{12}) = C_{11}$ S34

Longitudinal wave velocity $V_l = \sqrt{\frac{C_{11}}{\rho_x}}$ S35

Transverse wave velocity $V_t = \frac{V_l}{\sqrt{3}}$ S36

Rigidity modulus $G = \rho_x V_t^2$ S37

Poisson's ratio $\sigma = \frac{3B-2G}{6B+2G}$ S38

Young's modulus $E = (1+\sigma)2G$ S39

Mean wave velocity $V_m = \left(\frac{1}{3}\left(\frac{2}{V_t^3} + \frac{1}{V_l^3}\right)\right)^{-\frac{1}{3}}$ S40

where $K_{av} = (K_T + K_O)/2$ is the average force constant, a is the lattice parameter, and ρ_x is the X-ray density.

Table S9: Band position (υ), threshold energy (E_{th}), force constant (K), elastic parameters (C_{11}, B, V_l, V_t, V_m,G, σ, and E) and Debye temperature (Θ_D, θ_D) of the Co-A nanoparticles.

Parameters	Values
ν_A (cm^{-1})	578.61
ν_B (cm^{-1})	378.05
ν_{av} (cm^{-1})	478.33
ν_{th} (cm^{-1})	779.43
E_{th} x 10^{-2} (eV)	9.68
K_T (N/m)	144.28
K_O (N/m)	86.57
K_{av} (N/m)	115.43
C_{11}(GPa)	137.88
B (GPa)	137.88
V_l (m/s)	5.094 x 10^3
V_t (m/s)	2.941 x 10^3
V_m (m/s)	3.265 x10^3
G (Gpa)	45.95
σ	0.35
E (GPa)	124.07
Θ_D (K)	687.84
θ_D (K)	464.67

The corrected elastic moduli for zero porosity using Hasselman and Fulrath [33] models are given by:

$$\frac{1}{E_0} = \frac{1}{E}\left[1 - \frac{3p(1-\sigma)(9+5\sigma)}{2(7-5\sigma)}\right] \quad \text{S41}$$

$$\frac{1}{G_0} = \frac{1}{G}\left[1 - \frac{15p(1-\sigma)}{(7-5\sigma)}\right] \quad \text{S42}$$

$$\sigma_0 = \frac{E_0}{2G_0} - 1 \quad \text{S43}$$

$$B_0 = \frac{G_0 E_0}{3(3G_0 - E_0)} \quad \text{S44}$$

The elastic moduli have been corrected using the Ledbetter and Datta model [34] and are estimated by the following equations:

$$G_0 = \left(\frac{1}{2A_1}\right)\left[-A_2 + (A_2^2 - 4A_1A_3)^{\frac{1}{2}}\right] \quad \text{S45}$$

$$B_0 = \frac{4G_0B}{(4(1-P_o)G_0 - 3P_oB)} \quad \text{S46}$$

$$E_0 = \frac{9G_0B_0}{(G_0 - 3B_0)} \quad \text{S47}$$

$$A_1 = {}^{8}/_{3}(1 - P_o) \quad \text{S48}$$

$$A_2 = (3 - 2P_o)B - \left({}^{8}/_{3} + 4P_o\right)G \quad \text{S49}$$

$$A_3 = -3(1 + P_o)BG \quad \text{S50}$$

The elastic moduli corrected to zero porosity as a function of the pore fraction (P_o) are calculated for the prepared Co-A sample using the elastic model theory [35] according to the following equations:

$$V_l = V_{l0}(1 - C_lP_o) \quad \text{S51}$$

$$V_t = V_{t0}(1 - C_tP_o) \quad \text{S52}$$

$$E = E_0(1 - C_EP_o) \quad \text{S53}$$

$$G = G_0(1 - C_G P_o) \quad \text{S54}$$
$$\sigma = \sigma_0(1 - C_\sigma P_o) \quad \text{S55}$$

where C_l, C_t, C_E, C_G, and C_σ are constants of the materials. The nonporous elastic moduli are represented by the subscript '0'. The exact expressions for the constants are given below:

$$C_l = \frac{1}{2}\left(\left|\frac{(C_E + 2C_\sigma\sigma_0^2)(2-\sigma_0)}{(1-\sigma_0)(1+\sigma_0)(1-2\sigma_0)-1}\right|\right) \quad \text{S56}$$
$$C_t = \frac{1}{3} \quad \text{S57}$$
$$C_E = \frac{1}{18}(29 + 11\sigma_0) \quad \text{S58}$$
$$C_G = \frac{5}{3} \quad \text{S59}$$
$$C_\sigma = \left(\frac{5}{9}\right) + \left(\frac{11\sigma}{18}\right) - \left(\frac{1}{18}\sigma\right) \quad \text{S60}$$

Table S10: The elastic moduli of the nonporous Co-A nanoparticles.

Model	Parameters	Values
Hasselman and Fulrath model	E_0 (GPa)	237.29
	G_0(GPa)	82.62
	σ_0	0.44
	B_0(GPa)	618.26
Ledbetter and Datta model	E_0 (GPa)	218.17
	G_0 (GPa)	71.95
	B_0 (GPa)	330.25
	B_0/G_0	4.59
	A_1	2.03
	A_2	181.27
	A_3	-23549.37
Elastic model Theory	E_0 (GPa)	224.72
	G_0 (GPa)	76.37
	V_{l0} (m/s)	7433.92
	V_{t0}(m/s)	3195.58
	V_{m0} (m/s)	3610.85
	σ_0	0.43
	C_l	1.32
	C_E	1.87
	C_σ	0.79

The velocity of sound waves in solid and liquid media is determined using a thermodynamic equation given as [29, 30, 36]:

$$V^2 = \frac{-nm\gamma}{U_0} + \frac{R\gamma_T T}{M} \quad \text{S61}$$

where n and m are constants that define the potential energy function, γ_T is the specific heat ratio (C_p/C_v), R is the gas constant, T is the temperature, M is the molar mass, and U_0 is the potential energy. According to the above equation, the majority of ionic solids, including many spinel ferrite materials, have $\gamma_T \sim 1$, and n = 3. Here, V can be replaced with the mean sound velocity corrected to zero porosity (V_{m0}), and U_0 can be replaced with the polycrystalline solid lattice energy (U_L). Consequently, the lattice energy U_L reduces to the expression [29, 30]:

$$U_L = -3.108(M_W V_{m0}^2) \times 10^{-3}\ (eV) \quad \text{S62}$$

where M_W is the molecular weight of the ferrite sample.

The characteristic Debye temperature (θ_J) is computed using Waldron's methodology [26] and Modi's research [29,30] as:

$$\theta_J = \frac{hc\upsilon_{max}}{k_B} \quad \text{S63}$$

where the high-frequency cut-off of the elastic waves can be computed by applying Waldron's approach [26] using the equation $f_{max} = V_l \times \sigma_{max}$. The shortest wave is equivalent to one-half of the wave per mean interatomic distance, $\bar{d}$. As $\bar{d}$ is given by $\bar{d} = 1/4\ (3r_o + r_t) = 7.732\ (a/32)$, we obtain $\sigma_{max} = (2.07 \times 10^{-2})/a$ in (m).

Table S11 shows the predicted estimates of the high-frequency cut-off (f_{max}) for the prepared cobalt ferrite sample. The formula $\upsilon_{max} = f_{max}/C$ (m/s) provides the approximate means of the cut-off frequencies υ_1 and υ_3 of the oxide and metal ion vibrations, respectively. The values of the calculated high-frequency cut-off, σ_{max}, υ_{max}, and characteristic temperature of Debye θ_J are presented in **Table S11**.

Furthermore**,** the molar heat capacity at constant volume, C_v, is determined using θ_J. The C_v value at T = 300 K for the prepared Co-A spinel ferrite sample was computed using Einstein's theory [37] as:

$$C_V = 3p_T R \left(\frac{\theta_J}{T}\right)^2 \left(\frac{exp\left(\frac{\theta_J}{T}\right)}{\left(exp\left(\frac{\theta_J}{T}\right)-1\right)^2}\right) \quad \text{S64}$$

where p_T is the number of atoms per chemical formula, and R is the gas constant.

According to Dulong and Petit's law [37], the theoretically limiting heat capacity, $C_v = 21R$, for $A^{2+}B_2^{3+}O_4$ spinel ferrite system at constant volume and at $T = \theta_J$ is 174.5 J K^{-1} mol^{-1} [37].

Table S11: Thermodynamic parameters (lattice energy (U_L), shortest wave (σ_{max}), high-frequency cut-off (f_{max}), approximate mean elastic wave (ν_{max}), molar heat capacity at constant volume (C_v), molar heat capacity at constant pressure (C_P), and Debye temperature (θ_J) of the green-synthesized Co-A nanoparticles.

Parameters	U_L (eV)	$\sigma_{max} \times 10^7$ (m)	$f_{max} \times 10^{11}$ (s^{-1})	υ_{max} (m^{-1})	θ_J (K)	C_V ($J.K^{-1}.mol^{-1}$)	C_P ($J.K^{-1}.mol^{-1}$)
Values	-95.070	2.472	1.259	419.667	604.50	143.710	144.040

Raman Spectroscopy

Table S12: Raman vibrational data for eco-friendly Co-A nanoparticles with the assigned modes.

Parameters	Peak identity	Peak position (Exp)(cm^{-1})	peak position (reported)(cm^{-1})	FWHM (cm^{-1})	Area (cm^{-2})	Height (cm^{-1})
Values	$T_{2g}(1)$	200.27	198.00[38]	26.42	58.99	2.09
	$E_g(1)$	289.08	291.00[39]	56.74	403.29	6.68
	$E_g(2)$	352.82	335.00 [40]	23.44	88.22	2.75
	$T_{2g}(2)$	458.39	461.00[38]	77.86	1418.82	17.12
	$T_{2g}(3)$	523.96	520.00[41]	43.16	373.39	8.13
	$A_{1g}(2)$	591.66	600.00 [42]	82.90	1396.45	15.82
	$A_{1g}(1)$	669.94	670.54[43]	69.97	1544.64	20.73

High-resolution transmission electron microscope (HRTEM)

Table S13: Corresponding interplanar distances for the (220), (311), (400), (422), (511), (440), and (533) diffraction peaks of the Co-A nanoparticles obtained using XRD and HRTEM.

Miller indices (hkl)	d(Å) (XRD)	d(Å) (HRTEM)
220	2.958	2.945
311	2.523	2.513
400	2.092	2.089
422	1.708	1.713
511	1.611	1.622
440	1.479	1.488
533	1.276	1.278

X-ray photoelectron spectroscopy (XPS)

Table S14: Binding energy (BE, eV), peak assignment, full width at half maximum (FWHM), area, and area (%) of the constituents of the representative XPS emission for the Co-A sample.

Parameters	B.E (eV)	Peak Assignment	FWHM (eV)	Area CPS. (eV)	Area (%)	ΔE ($2P_{3/2}$-$2P_{1/2}$)
Co^{2+} $2P_{3/2}$	780.40	Octahedral Co^{2+}	3.37	**14860.69**	**40.40**	15.59 eV
	783.57	Tetrahedral Co^{2+}	3.37	**4438.91**	**12.07**	
	786.65	Shakeup Satellite	3.37	6037.41	16.42	
	789.49	Shakeup Satellite	3.37	3174.80	8.63	
Co^{2+} $2P_{1/2}$	-	-	-	-	-	
	795.99	Tetrahedral Co^{2+}	3.37	4896.90	13.31	
	801.67	Shakeup Satellite	3.37	1903.74	5.18	
	804.62	Shakeup Satellite	3.37	1466.12	3.99	
Fe^{3+} $2P_{3/2}$	710.58	Octahedral Fe^{3+}	2.90	**18068.74**	**28.73**	12.67 eV
	712.94	Tetrahedral Fe^{3+}	3.37	**11311.32**	**17.98**	
	716.07	Shakeup Satellite	3.37	5725.60	9.10	
	719.28	Shakeup Satellite	3.37	7061.73	11.23	
Fe^{3+} $2P_{1/2}$	723.25	Octahedral Fe^{3+}	3.37	7848.41	12.48	
	725.62	Tetrahedral Fe^{3+}	3.37	7544.23	11.99	
	728.99	Shakeup Satellite	3.37	2929.61	4.66	
	733.06	Shakeup Satellite	3.37	2405.11	3.82	
O1S	529.85	$CoFe_2O_4$	1.56	18166.41	69.35	-
	531 .00	C=O	3.38	8028.14	30.65	

Magnetic properties

Vibrating sample magnetometry (VSM) measurements

Table S15: Magnetic parameters for the Co-A nanoparticles.

Parameters	Values
$M_{s(+)}$ (emu/g)	67.907
$M_{s(-)}$ (emu/g)	-67.907
M_s (emu/g)	**67.907**
$M_{r(+)}$ (emu/g)	30.148
$M_{r(-)}$ (emu/g)	-30.292
M_r (emu/g)	**30.219**
η_B (μ_B)	2.853
η_{th} (μ_B)	3.920
$\alpha_{Y\text{-}K}$, (°)	29.088
M_r/M_s (R)	0.445
$H_{C(+)}$ (Oe)	1237.800
$H_{C(-)}$ (Oe)	-1228.800
H_C (Oe)	**1233.300**
K × 10^5 (erg/$cm^{3)}$	4.634
H_a (kOe)	**2.466**
H_{EB} (Oe)	**1.148**

The following formula [44] was used to calculate the effective magnetic moment η_B (Cal) per formula unit for the prepared Co-A sample:

$$\eta_B = \frac{M_W M_S}{5585} \quad \text{S65}$$

where M_W is the molecular weight of the spinel ferrite and M_S is the saturation magnetization.
It is known that Fe and Co have theoretical magnetic moments ((η_{Fe}) and (η_{Co})) of 5 and 3 μ_B, respectively.

Using Néel's collinear model, the magnetic moment per formula unit for such a system can be expressed as follows [45]:

$$\eta_{th} = M_B - M_A \quad \text{S66}$$

where M_A and M_B are the Bohr magnetons at the A and B sites, respectively.

The following equation can be used to determine the Yafet-Kittel angle:

$$\eta_B = M_B cos((\alpha_{Y\text{-}K})) - M_A \quad \text{S67}$$

where η_B is the observed magnetic moment and M_A and M_B are the magnetic moments at sites A and B, respectively.

The magnetocrystalline anisotropy constant and anisotropy field can be determined from the values of H_C and M_S according to the E. C. Stoner-Wohlfarth theory [46]:

$$H_C = \frac{0.98K_1}{M_S} \quad \text{S68}$$

The anisotropy field can also be calculated using the following equation [47]:

$$H_a = \frac{2K_1}{M_S} \quad \text{S69}$$

Furthermore, a discernible horizontal shift in the hysteresis loop is identified due to the occurrence of exchange bias. The exchange bias field is given by [48]:

$$H_{EB} = \frac{-[H_{(-)}+H_{(+)}]}{2} \quad \text{S70}$$

where $H_{(-)}$ and $H_{(+)}$ are the coercive field values in the negative and positive directions of the magnetic field, respectively.

Microwave high-frequency and switching field applications of nanoferrite

The following relation [49] can be used to evaluate the operating microwave frequency ω_m:

$$\omega_m = 8\pi^2\gamma M_S \quad \text{S71}$$

whereas M_s is the saturation magnetization of the cobalt ferrite samples, and γ = 2.8 MHz/Oe is the gyromagnetic ratio of the microwave ferrites.

The law of approach to saturation (LAS) is represented by [50]:

$$M = M_S\left(1 - \frac{a}{H} - \frac{b}{H^2}\right) + \kappa H \quad \text{S72}$$

The term (a/H) is associated with nonmagnetic factors such as structural defects, while the rotation of magnetization against magnetocrystalline anisotropy energy is represented by the term (b/H^2). κH, denoting forced magnetization, arises from spontaneous magnetization and increases linearly with the applied magnetic field.

Many research teams have computed the magneto-crystalline anisotropy constant for spinel ferrite materials using LAS to fit the high-field data, ignoring the terms a/H and κH and maintaining the term b/H^2 exclusively. This method has been previously reported [51]. In this study, the terms a/H and κH in Eq. (S72) are disregarded, and the simplified form of this equation is used to fit the observed magnetization data for the prepared Co-A sample for an applied magnetic field above 2 kOe.

Furthermore, the first magnetocrystalline anisotropy constant (K_1) (also called cubic anisotropy) is estimated using the fitting parameters Ms and b by the relation:

$$K_1 = \mu_O M_S\sqrt{\frac{105b}{8}} \quad \text{S73}$$

where μ_O is the permeability of free space, M_s is the saturation magnetization, and the constant b is dependent on the magnetocrystalline anisotropy constant K_1, $b = \left(\frac{8}{105}\right)\left(\frac{K_1^2}{\mu_O^2 M_S^2}\right)$, and the numerical coefficient (8/105) is due to the cubic anisotropy of the random polycrystalline samples. M_s and b (fitting parameters) are obtained from the fitted M-H curve.

Table S16: Magnetic parameters, including the switching distribution field (SDF), the peak positions of the SFD curve (H_M), (dM/dH) at H = 0 and at H_M, K_1 and M_s of the Co-A nanoparticles.

Parameter	SFD (Oe)	H_M (Oe)	dM/dH (emu/g×10^{-3})		M_s (emu/g)	K_1×10^6 (erg/cm^3)
			H_0	H_M		
Values	3.08	1522.42	19	32	69.90	3.94

Magnetocaloric effect (MCE)

Magnetic entropy change

Maxwell's relation can be given as[52]:

$$\Delta S_M(T,\Delta H) = \mu_o \int_{H1}^{H2} \left(\frac{\partial M(T,H)}{\partial T}\right)_H dH \quad \text{S74}$$

where H and μ_o are the magnetic field intensity and the permeability of the free space, respectively.

For small discrete magnetic fields and temperature intervals, the Maxwell equation is approximated for determining the magnetic entropy change and given by [45]:

$$\left|\Delta S_M\left(\frac{T_i+T_{i+1}}{2}\right)\right| = \sum \left(\frac{(M_i-M_{i+1})H_i}{T_{i+1}-T_i}\right)\Delta H_i \quad \text{S75}$$

where M_i and M_{i+1} are the experimental data of magnetization measured at temperatures T_i and T_{i+1}.

Mössbauer spectroscopy

Table S17: Isomer shift δ (IS), quadrupole splitting (QS), hyperfine magnetic field (H_{hf}), area percentage, line width (Γ), cation distribution, inversion parameter (x), and area ratio of tetrahedral and octahedral sites of Fe^{3+} ions of the eco-friendly Co-A nanoparticles derived from Mössbauer spectra recorded at room temperature.

Parameters	Sextet	δ (IS) (mm/s)	QS (mm/s)	H_{hf} (T)	%Area	Γ(G) (mm/s)	A_{Td}/A_{Oh}	Site/phase assignment
Values	A	0.282	0.009	48.370	43.000	0.117	0.754	Tetrahedral
	B1	0.385	0.005	50.867	38.500	0.121		Octahedral
	B2	0.341	-0.046	46.997	18.500	1.033		Octahedral
Error		±0.0583	±0.0223	±2.3629	±13.3599	±0.5330		
Cation distribution		$(Co_{0.228}Fe_{0.772})_A(Co_{0.772}Fe_{1.228})_B$						
Inversion parameter (x)		0.772						

Optical properties

Diffuse reflectance spectroscopy (DRS)

When evaluating the optical energy gap using UV–VIS–NIR diffuse reflectance spectra, the Kubelka–Munk theory utilizes the Kubelka–Munk function (F(R)), which is expressed by the following equation [53]:

$$F(R) = \frac{\alpha}{S} = \frac{(1-R)^2}{2R} \quad \text{S76}$$

where R represents diffuse reflectance, α is the absorption coefficient, S is the scattering factor, and F(R) is the Kubelka–Munk function.

The optical band gap (E_g) is determined through the relation:

$$F(R)\, h\nu = B\,(h\nu - E_g)^{1/n} \quad \text{S77}$$

where B and E_g are energy-independent constant and the optical band gap, respectively, and n is a constant that can take the values n = 2 for the indirect allowed transition and n = 1/2 for the direct allowed transition.

Brunauer–Emmett–Teller (BET) surface area analysis

The values of the BET constant (C) and the volume of the monolayer of adsorbate (V_m) were determined from the linear fit of the prepared sample using specific equations. These values were obtained using the slope (A) and intercept (I) derived from the BET plot using the following equations [54].

$V_m = 1 / (A + I)$ S78

$C = 1 + (A/I)$ S79

where A and I are the slope and intercept of the BET plot, respectively.

Table S18: Quantity of monolayer adsorbed gas (V_m), BET constant, slope (A), intercept (I), and surface area of the Co-A nanoparticles extracted from BET analysis.

Parameter	V_m (cm^3)/g	BET constant	A	$I \times 10^{-4}$	Surface area (m^2/g)
Value	79.670	20.005	0.012	6.314	347.040

Heavy metal removal

Table S19: Comparison of the highest adsorption capacities for heavy metal ions of the eco-friendly synthesized Co-A nanoparticles with other reported adsorbents.

Adsorbent	Adsorbate	Removal efficiency%	Reference
Ni-doped magnetite	Pb^{2+}	73	[55]
$CoFe_2O_4$/0.02GR	Pb^{2+}	99	[56]
$CoFe_2O_4$	Pb^{2+}	100	[57]
$CoFe_2O_4$	Cr^{3+}	96	
$CoFe_2O_4$	Pb^{2+}	100	The present work
$CoFe_2O_4$	Cr^{3+}	100	

One-way ANOVA

Table S20: One-way ANOVA of the adsorption efficiency%.

Cr^{3+}						
Source of Variation	*SS*	*df*	*MS*	*F*	*F_{cri}*	*P -Value*
Between groups	*3481*	*2*	*1740.51*	*6.64*	*3.63*	***0.008***
Within groups	*4197*	*16*	*262.29*			
Total	*7678*	*18*				
Pb^{2+}						
Source of Variation	*SS*	*df*	*MS*	*F*	*F_{cri}*	*P -Value*
Between groups	*1754*	*2*	*827.21*	*6.11*	*3.63*	***0.011***
Within groups	*2167*	*17*	*135.47*			
Total	*3821*	*19*				

Tukey's HSD pairwise comparison

Table S21: Grouping information using the Tukey HSD test and 95% confidence intervals.

Factors		*N*	*Mean*	*Grouping*	
Removal% Cr^{3+}					
Dose of adsorbent	*Group 1*	*6*	*91.27*	*A*	
Contact time	*Group 2*	*6*	*85.68*	*A*	
PH	*Group 3*	*7*	*60.79*		*B*
Removal% Pb^{2+}					
Dose of adsorbent	*Group 1*	*6*	*95.49*	*A*	
Contact time	*Group 2*	*6*	*92.26*	*A*	
PH	*Group 3*	*7*	*75.00*		*B*

Photo-Fenton Catalytic Activity

Table S22: Performance comparison of the highest degradation efficiency of the present Co-A nanoparticles with that of other reported catalysts [58].

Catalyst	Irradiation	Dose of Catalyst (g/L)	Type of Dye: Conc	Oxidizer	Degradation Efficiency (%) Rate constant	Time (min)	Ref
$CoFe_2O_4$	Visible	1	RhB 10 ppm	1.5 ml H_2O_2 30%	90.6, k=0.5 h^{-1}	270	[59]
$CoFe_2O_4$	UVA	2	MB 3.5×10^{-5} M L^{-1}	$H_2C_2O_4$ 10^{-3} M L^{-1}	72, k=3.68 h^{-1}	25	[60]
$CoFe_2O_4$	UVA	0.2	MB 3.5×10^{-5} M L^{-1}	$H_2C_2O_4$ 10^{-3} M L^{-1}	95, k=3.16 h^{-1}	60	[60]
$CoFe_2O_4$	Visible	0.15	MB 9.37×10^{-5} M L^{-1}	$H_2C_2O_4$ 10^{-3} M L^{-1}	96.88, k=3.20 h^{-1}	60	The present work

Antibacterial test

Table S23: Performance comparison of the antibacterial activity of the present Co-A nanoparticles with that of other reported plant-mediated $CoFe_2O_4$ nanoparticles.

Pathogen name	Plant name	Conc of $CoFe_2O_4$	Part of the plant	ZOI (mm)	Reference
Staphylococcus aureus -9779	Hibiscus rosa sinensis	10 mg/ml	Leaves	9	[61]
Escherichia coli-745				12	
Staphylococcus aureus (ATCC 6538)	Eucalyptus	10 mg/ml	Leaves	8.5	[62]
Enterococcus faecalis (ATCC 29212)				**0**	
Escherichia coli (ATCC 25922)				7.5	
Staphylococcus aureus (96)	Okra	0.1 mg/ml	Pulp	14	[63]
Escherichia coli (ATCC 8739)	Apple	0.1 mg/ml	Pulp	26	The present work
K. pneumoniae (ATCC 13883)				28	
Staphylococcus aureus (ATCC 6538)				29	
Enterococcus faecalis (ATCC 29212)				30	

References

1. Ahmed, M., et al., *Removing lead ions from water by using nanocomposite (rare earth oxide/alumina).* Journal of Molecular Liquids, 2017. **240**: p. 604-612.
2. Ichipi, E.O., et al., *Fabrication and characterization of recyclable, magnetic (CoFe2O4) x/Ag2S-ZnO composites for visible-light-induced photocatalytic degradation of methylene blue dye.* Journal of Water Process Engineering, 2023. **54**: p. 104040.
3. Abbas, Y.M., et al., *Investigation of structural and magnetic properties of multiferroic La1-xYxFeO3 Perovskites, prepared by citrate auto-combustion technique.* Journal of Magnetism and Magnetic Materials, 2019. **482**: p. 66-74.
4. Bhagwat, M., et al., *Rietveld refinement study of nanocrystalline copper doped zirconia.* Materials research bulletin, 2003. **38**(13): p. 1713-1724.
5. Fuster, V., et al., *Characterization of phases in an Fe–Mn–Si–Cr–Ni shape memory alloy processed by different thermomechanical methods.* Materials Characterization, 2015. **109**: p. 128-137.
6. Bharati, V., et al., *Influence of trivalent Al–Cr co-substitution on the structural, morphological and Mössbauer properties of nickel ferrite nanoparticles.* Journal of Alloys and Compounds, 2020. **821**: p. 153501.
7. Kulkarni, A. and S. Mathad, *Synthesis and structural analysis of Co–Zn–Cd ferrite by Williamson–Hall and size–strain plot methods.* International Journal of Self-Propagating High-Temperature Synthesis, 2018. **27**: p. 37-43.
8. Tatarchuk, T., et al., *Structural characterization and antistructure modeling of cobalt-substituted zinc ferrites.* Journal of Alloys and Compounds, 2017. **694**: p. 777-791.
9. Paswan, S.K., et al., *Optimization of structure-property relationships in nickel ferrite nanoparticles annealed at different temperature.* Journal of Physics and Chemistry of Solids, 2021. **151**: p. 109928.
10. Kugimiya, K. and H. Steinfink, *Influence of crystal radii and electronegativities on the crystallization of AB2X4 stoichiometries.* Inorganic Chemistry, 1968. **7**(9): p. 1762-1770.
11. Monisha, P., et al., *Influence of Mn dopant on the crystallite size, optical and magnetic behaviour of CoFe2O4 magnetic nanoparticles.* Journal of Physics and Chemistry of Solids, 2021. **148**: p. 109654.
12. Chandramohan, P., et al., *Cation distribution and particle size effect on Raman spectrum of CoFe2O4.* Journal of Solid State Chemistry, 2011. **184**(1): p. 89-96.
13. Vara Prasad, B., K. Ramesh, and A. Srinivas, *Structural and magnetic studies of nano-crystalline ferrites MFe 2 O 4 (M= Zn, Ni, Cu, and Co) synthesized via citrate gel autocombustion method.* Journal of superconductivity and Novel magnetism, 2017. **30**: p. 3523-3535.
14. Lakhani, V., et al., *Structural parameters and X-ray Debye temperature determination study on copper-ferrite-aluminates.* Solid State Sciences, 2011. **13**(3): p. 539-547.
15. Arean, C.O., et al., *Crystal chemistry of cadmium-zinc ferrites.* Journal of solid state chemistry, 1988. **77**(2): p. 275-280.
16. Dhiman, R., S. Taneja, and V. Reddy, *Preparation and characterization of manganese ferrite aluminates.* Advances in Condensed Matter Physics, 2008. **2008**.
17. Kumar, R., et al., *Experimental and theoretical verification of cation distribution and spin canting effect via structural and magnetic studies of NiZnCo ferrite nanoparticles.* Journal of the Australian Ceramic Society, 2022: p. 1-11.
18. Mazen, S., et al., *The effect of titanium on some physical properties of CuFe2O4.* physica status solidi (a), 1992. **134**(1): p. 263-271.
19. Somvanshi, S.B., et al., *Structural, thermal, spectral, optical and surface analysis of rare earth metal ion (Gd3+) doped mixed Zn–Mg nano-spinel ferrites.* Ceramics International, 2020. **46**(9): p. 13170-13179.
20. Barrett, C., *Massalski., TB Structure of Metals*. 1980, Pergamon Press: Oxford, UK.

21. Caglar, M., Y. Caglar, and S. Ilican, *The determination of the thickness and optical constants of the ZnO crystalline thin film by using envelope method.* Journal of optoelectronics and advanced materials, 2006. **8**(4): p. 1410.
22. Varchola, M., et al., *Structural Analysis of Dispersion Strengthened Al-Al4C3 Material by XRD Method.* 2011.
23. Mahmoud, M.H., et al., *Synthesis of highly ordered 30 nm NiFe2O4 particles by the microwave-combustion method.* Journal of magnetism and magnetic materials, 2014. **369**: p. 55-61.
24. Bouokkeze, D., et al., *Investigation of the structural, optical, elastic and electrical properties of spinel LiZn 2 Fe 3 O 8 nanoparticles annealed at two distinct temperatures.* RSC advances, 2019. **9**(70): p. 40940-40955.
25. Chandekar, K.V. and K.M. Kant, *Size-strain analysis and elastic properties of CoFe2O4 nanoplatelets by hydrothermal method.* Journal of Molecular Structure, 2018. **1154**: p. 418-427.
26. Waldron, R., *Infrared spectra of ferrites.* Physical review, 1955. **99**(6): p. 1727.
27. Bhatu, S., et al., *Effect of nickel substitution on structural, infrared and elastic properties of lithium ferrite.* 2007.
28. Bouhadouza, N., et al., *Structural and vibrational studies of NiAlxFe2− xO4 ferrites (0≤ x≤ 1).* Ceramics international, 2015. **41**(9): p. 11687-11692.
29. Modi, K., et al., *Infrared spectral evolution, elastic, optical and thermodynamic properties study on mechanically milled Ni0. 5Zn0. 5Fe2O4 spinel ferrite.* Journal of Molecular Structure, 2013. **1049**: p. 250-262.
30. Modi, K.B., et al., *Raman and Mossbauer spectroscopy and X-ray diffractometry studies on quenched Copper–Ferri–Aluminates.* Inorganic chemistry, 2015. **54**(4): p. 1543-1555.
31. Mohammed, K., et al., *Infrared and structural studies of Mg1–xZnxFe2O4 ferrites.* Physica B: Condensed Matter, 2012. **407**(4): p. 795-804.
32. Yadav, R.S., et al., *Effects of annealing temperature variation on the evolution of structural and magnetic properties of NiFe2O4 nanoparticles synthesized by starch-assisted sol–gel auto-combustion method.* Journal of Magnetism and Magnetic Materials, 2015. **394**: p. 439-447.
33. Hasselman, D. and R. Fulrath, *The effect of a small fraction of spherical porosity on the elastic moduli of glass.* 1963.
34. Sharma, P. and K. Modi, *Effect of Fe3+ substitution on elastic properties of yttrium iron garnet.* Physica Scripta, 2010. **81**(1): p. 015601.
35. Rice, R.W., *Microstructure dependence of mechanical behavior of ceramics*, in *Treatise on materials science & technology*. 1977, Elsevier. p. 199-381.
36. Modi, K., M. Chhantbar, and H. Joshi, *Study of elastic behaviour of magnesium ferri aluminates.* Ceramics international, 2006. **32**(2): p. 111-114.
37. De Podesta, M., *Understanding the properties of matter*. 2002: CRC Press.
38. Yadav, R.S., et al., *Impact of grain size and structural changes on magnetic, dielectric, electrical, impedance and modulus spectroscopic characteristics of CoFe2O4 nanoparticles synthesized by honey mediated sol-gel combustion method.* Advances in Natural Sciences: Nanoscience and Nanotechnology, 2017. **8**(4): p. 045002.
39. Kumar, Y., A. Sharma, and P.M. Shirage, *Impact of different morphologies of CoFe2O4 nanoparticles for tuning of structural, optical and magnetic properties.* Journal of Alloys and Compounds, 2019. **778**: p. 398-409.
40. Jovanović, S., et al., *Effect of oleic acid concentration on the physicochemical properties of cobalt ferrite nanoparticles.* The Journal of Physical Chemistry C, 2014. **118**(25): p. 13844-13856.
41. Ansari, S.M., et al., *Eco-friendly synthesis, crystal chemistry, and magnetic properties of manganese-substituted CoFe2O4 nanoparticles.* ACS omega, 2020. **5**(31): p. 19315-19330.
42. Sagu, J.S., K. Wijayantha, and A.A. Tahir, *The pseudocapacitive nature of CoFe2O4 thin films.* Electrochimica Acta, 2017. **246**: p. 870-878.
43. Ansari, S.M., et al., *Particle size, morphology, and chemical composition controlled CoFe2O4 nanoparticles with tunable magnetic properties via oleic acid based solvothermal synthesis for application in electronic devices.* ACS Applied Nano Materials, 2019. **2**(4): p. 1828-1843.

44. Karimi, S., et al., *Effects of Zn-Cr-substitution on the structural and magnetic properties of Ni1− xZnxFe2− xCrxO4 ferrites.* Ceramics International, 2016. **42**(15): p. 16948-16955.
45. Humbe, A.V., et al., *Cation distribution, magnetic and hyperfine interaction studies of Ni–Zn spinel ferrites: role of Jahn Teller ion (Cu 2+) substitution.* Materials Advances, 2020. **1**(4): p. 880-890.
46. Wahba, A.M. and M.B. Mohamed, *Structural, magnetic, and dielectric properties of nanocrystalline Cr-substituted Co0. 8Ni0. 2Fe2O4 ferrite.* Ceramics International, 2014. **40**(4): p. 6127-6135.
47. Ramadan, R. and M.M. El-Masry, *Effect of (Co and Zn) doping on structural, characterization and the heavy metal removal efficiency of CuFe2O4 nanoparticles.* Journal of the Australian Ceramic Society, 2023: p. 1-16.
48. Singh, R.P., C. Tomy, and A. Grover, *Observation of tunable exchange bias in Sr2YbRuO6.* Applied Physics Letters, 2010. **97**(18).
49. Kuo, M.-F., et al., *Structure and magnetic properties of Mn and Al doped magnesium ferrite.* China Steel Technical Report, 2016. **29**: p. 44-48.
50. Chikazumi, S., *Physics of ferromagnetism*. 1997: Oxford university press.
51. Devi, E.C. and I. Soibam, *Magnetic properties and law of approach to saturation in Mn-Ni mixed nanoferrites.* Journal of Alloys and Compounds, 2019. **772**: p. 920-924.
52. Ferenc, J., et al., *Entropy Change Calculations for Pure Gd and a Ni-Mn-Cu-Ga Heusler Alloy: Constant Field vs. Constant Temperature Experiment.* Acta Physica Polonica A, 2015. **128**(1): p. 111-115.
53. Raddaoui, G., et al., *Investigation studies of structural, electrical, dielectric, and optical of DyTi0. 5 Mn0. 5O3 multiferroic for optoelectronics applications.* Journal of Materials Science: Materials in Electronics, 2022. **33**(27): p. 21890-21912.
54. Lal, G., et al., *Rietveld refinement, Raman, optical, dielectric, Mössbauer and magnetic characterization of superparamagnetic fcc-CaFe2O4 nanoparticles.* Ceramics International, 2019. **45**(5): p. 5837-5847.
55. Ramadan, R., *Preparation, characterization and application of Ni-doped magnetite.* Applied Physics A, 2019. **125**(9): p. 586.
56. Ateia, E.E., R. Ramadan, and A.S. Shafaay, *Efficient treatment of lead-containing wastewater by CoFe2O4/graphene nanocomposites.* Applied Physics A, 2020. **126**(3): p. 222.
57. Hussein, H., S. Ibrahim, and S.A. Khairy, *Biosynthesis of CoFe2O4 ferrite nanoparticles using Greek yogurt solution: Deep structural insights and appraisal for ecological mitigation via quartz crystal microbalance.* Journal of Water Process Engineering, 2024. **65**: p. 105856.
58. Hussein, H., S. Ibrahim, and S.A. Khairy, *Sustainable synthesis of CoFe2O4 nanoparticles with tailored physical properties using Hibiscus extract for photo-Fenton catalytic degradation of methylene blue dye: Response surface methodology.* Journal of Water Process Engineering, 2025. **76**: p. 107893.
59. To Loan, N.T., et al., *CoFe2O4 nanomaterials: effect of annealing temperature on characterization, magnetic, photocatalytic, and photo-fenton properties.* Processes, 2019. **7**(12): p. 885.
60. Ngoc, H.L.T., et al., *Effect of annealing temperature on phase transitions and photo-Fenton catalytic activity of CoFe2O4 nanopowder.* Journal of Physics and Chemistry of Solids, 2023. **178**: p. 111366.
61. Velayutham, L., et al., *Photocatalytic and antibacterial activity of CoFe2O4 nanoparticles from Hibiscus rosa-sinensis plant extract.* Nanomaterials, 2022. **12**(20): p. 3668.
62. Gingasu, D., et al., *Synthesis of CoFe2O4 through wet ferritization method using an aqueous extract of eucalyptus leaves.* Coatings, 2023. **13**(7): p. 1250.
63. Kombaiah, K., et al., *Okra extract-assisted green synthesis of CoFe2O4 nanoparticles and their optical, magnetic, and antimicrobial properties.* Materials Chemistry and Physics, 2018. **204**: p. 410-419.